Impact of local atmospheric intraseasonal variability on mean sea ice state in the Arctic Ocean

Xi Liang[1], Chengyan Liu[2*], Lejiang Yu[2,3], Martin Losch[4], Lujun Zhang[5], Xichen Li[6], Fu Zhao[1], Zhongxiang Tian[1]

[1]Key Laboratory of Marine Hazards Forecasting, National Marine Environmental Forecasting Center, Ministry of Natural Resources, Beijing, China.

[2]Southern Marine Science and Engineering Guangdong Laboratory (Zhuhai), China

[3]Polar Research Institute of China, Shanghai, China.

[4]Alfred-Wegener-Institut, Helmholtz Zentrum für Polar- und Meeresforschung, Bremerhaven, Germany.

[5]CMA-NJU Joint Laboratory for Climate Prediction Studies, School of Atmospheric Sciences, Nanjing University, Nanjing, China.

[6]International Center for Climate and Environment Sciences, Institute of Atmospheric Physics, Chinese Academy of Sciences, Beijing, China.

Corresponding author: Chengyan Liu (liuchengyan@sml-zhuhai.cn)

Abstract

The Arctic atmosphere shows significant variability on intraseasonal timescales of 10-90 days. The intraseasonal variability in the Arctic sea ice is clearly related to that in the Arctic atmosphere. It is well-known that the Arctic mean sea ice state is governed by the local mean atmospheric state. However, the response of the Arctic mean sea ice state to the local atmospheric intraseasonal variability is unclear. The Arctic atmospheric intraseasonal variability exists in both the thermodynamical and dynamical variables. Based on a sea ice-ocean coupled simulation with a quantitative sea ice budget analysis, this study finds that: 1) the intraseasonal atmospheric thermodynamical variability tends to reduce sea ice melting through changing the downward heat flux on the open water area in the marginal sea ice zone, and the intraseasonal atmospheric dynamical variability tends to increase sea ice melting by a combination of modified air-ocean, ice-ocean heat fluxes and sea ice deformation. 2) The intraseasonal atmospheric dynamical variability increases summertime sea ice concentration in the Beaufort Sea and the Greenland Sea but decreases summertime sea ice concentration along the Eurasian continent in the East Siberia-Laptev-Kara Seas, resulting from the joint effects of the modified air-ocean, ice-ocean heat fluxes, the sea ice deformation, as well as the mean sea ice advection due to the changes of sea ice drift. The large spread in sea ice in the CMIP models may be partly attributed to the different model performances in representing the observed atmospheric intraseasonal variability. Reliable modeling of atmospheric intraseasonal variability is an essential condition in correctly projecting future sea ice evolution.

Key words: Arctic sea ice, intraseasonal atmospheric variability, sea ice budget

1. Introduction

The Arctic sea ice extent has declined substantially in the past several decades under greenhouse warming (Comiso, 2012; Gao et al., 2015). According to the National Snow and Ice Data Center (NSIDC) Sea Ice Index (Fetterer et al., 2017), the Arctic sea ice fell to its second-lowest September extent on record on 15 September 2020, just 0.4×10^6 km^2 larger than the minimum record of 3.39×10^6 km^2 in 2012 (Francis, 2013). With the relative amount of first year ice increasing and more open water exposed to the warming atmosphere, the Arctic sea ice and ocean states are expected to be more sensitive to local atmospheric forcing (Meier et al., 2014).

The atmospheric variability on annual to decadal timescales in the Arctic region is dominated by two dominant modes: the Arctic Oscillation (AO; Thompson and Wallace, 1998) and the Arctic Dipole (AD; Wang et al., 2009). Sea ice responds primarily to atmospheric forcing, therefore the long term variability of the Arctic sea ice features oscillations reminiscient of the AO and AD modes (Deser et al., 2000; Belchansky et al., 2004; Koenigk et al., 2009; Strong, 2012; Frankignoul et al., 2014). Sea ice export through the Fram Strait shows a high correlation with the AO index after the late 1970s (Kwok and Rothrock, 1999). Watanabe et al. (2006) pointed out that the AD plays an important role in sea ice export from the Arctic Ocean to the Greenland Sea due to its strong meridionality. Furthermore, the 2007 sea ice extent minima was partly driven by the positive phase of the summertime AD, which favored an enhanced northerly wind over the Nordic Sea pushing sea ice toward the Fram Strait (Wang et al., 2009). The change in the AD and AO have also been linked to the

Arctic sea ice variations and the recent declining trend (Rigor et al., 2002; Deser and Teng, 2008; Notz, 2015; Yu and Zhong, 2018). Ding et al. (2017) show that the September sea ice extent decline since 1979 may be largely attributed to the long-term trends in high-latitude summertime atmospheric circulation. Yu and Zhong (2018) suggested that the anomalous autumn AD and AO modes could explain as much as 50% of autumn sea ice decline between 1979 and 2016.

Aside from the remarkable long term variability, the intraseasonal variability of the Arctic sea ice was also highlighted in previous studies. Indeed, Fang and Wallace (1994) have already found that the Arctic sea ice concentration responds to atmospheric forcing on the timescale of a few weeks. From satellite-retrieved sea ice concentration data, previous studies have clearly identified the intraseasonal variation of the Arctic sea ice on timescales of 10-90 days. Henderson et al. (2014) proposed that the Arctic sea ice variance features intraseasonal oscillation both in summer and winter seasons. Qian et al. (2020) found that sea ice concentration in the Arctic marginal seas exhibits remarkable intraseasonal variations with dominant periods of 40-60 days and 70-80 days in summer, and they noted that the strong intraseasonal signal of Arctic sea area anomalies is accompanied with a northward retreat of the sea ice edge before summer and a southward advance after summer.

The intraseasonal variability of the Arctic sea ice is primarily controlled by the local atmospheric intraseasonal variability. It is widely recognized that the Arctic mean sea ice state is governed by the local mean atmospheric state. However, the response of the Arctic mean sea ice state to the local atmospheric intraseasonal variability remains unclear. The Arctic atmospheric intraseasonal variability exists in both the thermodynamical and dynamical variables. In this study, we analyze the sea ice responses to the prescribed atmospheric forcing in a coupled regional sea ice-ocean model, and quantitatively diagnose the thermodynamical and dynamical contribution of the atmospheric forcing with numerical simulations.

This paper is organized as follows: section 2 describes the sea ice-ocean model, the processing of the prescribed atmospheric forcing fields, and the experiment design. Section 3 evaluates the result of the atmospheric forcing data processing. Section 4 presents the responses of the simulated sea ice mean state, the involved physical mechanism based on the quantitative sea ice budget analysis, as well as the responses of the modeled sea ice intraseasonal variability. Discussion and conclusion are shown in section 5.

2. Method

2.1 The Arctic Regional Sea Ice-Ocean Coupled Model

The Arctic sea ice-ocean model used in this study is an Arctic configuration of the Massachusetts Institute of Technology general circulation model (MITgcm; Marshall et al., 1997). The model grid is configured on the curvilinear coordinates with an average horizontal resolution of 18 km (Nguyen et al., 2011). The model domain covers the whole Arctic Ocean with its open boundaries close to 55 °N in both the Atlantic and Pacific sectors. The ocean model includes a horizontal grid distribution of 420 × 384 points and 50 vertical layers, with 28 vertical levels in the upper 1000 m depth. The top layer thickness of the ocean model is 10 m.

The sea ice model is based on the viscous-plastic rheology and the zero-layer snow/ice thermodynamics with a prescribed sub-grid ice thickness distribution process with 7 thickness categories (Hibler, 1984; Losch et al., 2010). The sea ice momentum equations are solved following Zhang and Hibler (1997). The sea ice model shares the horizontal grid with the ocean model. The topographical data are from the U. S. National Geophysical Data Center 2 min global relief data set (Smith and Sandwell, 1997). The open boundary conditions are climatological monthly fields derived from the project Estimating the Circulation and Climate of the Ocean phase Ⅱ: high resolution global ocean and sea ice data synthesis (Menemenlis et al., 2008), which includes potential temperature, salinity, current and sea surface elevation. The initial ocean temperature/salinity field is a climatological field derived from the World Ocean Atlas 2005 (Locarnini et al., 2006; Antonov et al., 2006). Monthly mean river runoff is from the Arctic Runoff Data Base (Nguyen et al., 2011). The configuration of this coupled sea ice-ocean model can also be found in Liang and Losch (2018) in more detail.

2.2 Atmospheric Data Processing

The model is forced by atmospheric data derived from the 3-hourly Japanese 55-year Reanalysis (JRA55) data during 1979 to 2013 (Kobayashi et al., 2015; Harada et al., 2016), which includes 7 atmospheric variables: the 2 m air temperature (*TEMP*), the 2 m air specific humidity (*HUMI*), the 10 m wind (the zonal and meridional components; *UWND* and *VWND*), the precipitation (*RAIN*), and the downward surface shortwave and longwave radiative heat fluxes (*SWHF* and *LWHF*). To simplify the description of atmospheric data processing, we define a symbol $VAR_{79\text{-}13}$ (*VAR* includes *TEMP*, *HUMI*, *UWND*, *VWND*, *RAIN*, *SWHF*, and *LWHF*) to denote the above-mentioned variables.

The following procedures are carried out to process the 7 atmospheric variables from the JRA55 on every horizontal grid (see Table 1 for the detailed information of the abbreviations defined below): 1) the climatological annual cycle data with 3 hourly temporal intervals expressed by the symbol VAR_{Ac}, which are used to spin up the coupled Arctic sea ice-ocean model, are derived by averaging the values at the corresponding time in all the years from 1979 to 2013. The last days in leap years are simply excluded. 2) The residual after removing the climatological annual cycle component (VAR_{Ac}) from the original data ($VAR_{79\text{-}13}$) is called as the VAR_{woAc}. An order one polynomial fit is applied to VAR_{woAc} to get the long-term trend (VAR_{Gw}) induced by global warming. We remove the VAR_{Gw} from VAR_{woAc} to get the residual VAR_{woAcGw}. Then, the climatological annual cycle component (VAR_{Ac}) is added cyclically to the VAR_{woAcGw} to get the 35-years atmospheric forcing without the global warming signal (VAR_{woGw}) in the whole domain. 3) We use a band-stop filter algorithm based on a Chebyshev Type I filter to eliminate the oscillations with periods between 10 days and 90 days in the regions north of 60 °N in VAR_{woAcGw}, and the residual is denoted by $VAR_{woAcGwIs}$. Then the climatological annual cycle component (VAR_{Ac}) is added cyclically to the $VAR_{woAcGwIs}$ to get the 35-years atmospheric forcing VAR_{woGwIs} which excludes global warming signal in whole domain and intraseasonal oscillation components in the regions north of 60 °N.

2.3 Experiment Design

Initialized from the climatological temperature/salinity field and the ocean at rest, the model is integrated for 20 years with the climatological annual cycle forcing of VAR_{Ac}. The model reaches a quasi-equilibrium status after 10-years of spin-up (not shown). Four different simulations are started from the ocean and sea ice state on the last day of the 20-years period.

The four simulations CONTROL, WOISALL, WOISTHE, WOISDYN (Table 2), use the same configuration except for the atmospheric forcing conditions. The CONTROL run is forced by the 3 hourly JRA55 variables without the global warming signal in whole domain (VAR_{woGw}). The WOISALL (WithOut IntraSeasonal variability in ALL atmospheric variables) run is forced by the 3 hourly JRA55 variables without the global warming signal, and without intraseasonal variability in the regions north of 60 °N (VAR_{woGwIs}). The WOISTHE (WithOut IntraSeasonal variability in atmospheric THErmodynamical variables) run is forced by the 3 hourly JRA55 dynamical variables without the global warming signal ($UWND_{woGw}$, $VWND_{woGw}$, $RAIN_{woGw}$), and the thermodynamical variables also without the intraseasonal variability in the regions north of 60 °N ($TEMP_{woGwIs}$, $HUMI_{woGwIs}$, $SWHF_{woGwIs}$, $LWHF_{woGwIs}$). The WOISDYN (WithOut IntraSeasonal variability in atmospheric DYNamical variables) run is forced by the 3 hourly JRA55 thermodynamical variables without the global warming signal ($TEMP_{woGw}$, $HUMI_{woGw}$, $SWHF_{woGw}$, $LWHF_{woGw}$), and the dynamical variables also without the intraseasonal variability in the regions north of 60 °N ($UWND_{woGwIs}$, $VWND_{woGwIs}$, $RAIN_{woGwIs}$). The WOISDYN/WOISTHE run differs from the CONTROL run in that whether the intraseasonal variability in local atmospheric dynamical/thermodynamical variables are removed, while the intraseasonal variability in all local atmospheric variables are removed in the WOISALL run. Based on the comparison between these four simulations, we can quantify the relative contribution of the local atmospheric intraseasonal variability in the thermodynamical variables or/and that in the dynamical variables on the evolution of the Arctic sea ice states. Each simulation is run for 35 years and daily averages are stored. The last 30 years of model output of each simulation are analyzed. It is worth noting that we classify the precipitation as dynamical variable because the precipitation can affect upper ocean stratification and ocean currents, and has indirect effects on the sea ice drift. However this setting is crude, because solid precipitation, i. e. snow, on the ice surface also has a large effect on the ice surface heat budget by increasing the surface albedo and decreasing the heat conductivity.

3. Verification of Atmospheric Data Processing

To assess the atmospheric data processing method used in section 2.2, we apply an EOF analysis to the daily 2 m air temperature anomalies derived from $TEMP_{woGw}$ used in the CONTROL run (Figure 1a, 1b) and those derived from $TEMP_{woGwIs}$ used in the WOISALL run (Figure 1c, 1d). A power spectrum analysis is applied to the time series of the leading EOF modes of the daily 2 m air temperature anomalies derived from $TEMP_{woGw}$ used in the CONTROL run (Figure 2a, 2b) and those derived from $TEMP_{woGwIs}$ used in the WOISALL (Figure 2c, 2d) run. In the atmospheric forcing variable $TEMP_{woGw}$, the first-leading mode has the typical AO pattern of the periodic oscillation of the atmospheric mass in polar regions (Figure 1a), and the second mode presents the AD pattern of the opposite trends of the atmospheric mass over the Eurasian Arctic and the Beaufort-North America-Greenland regions (Figure 1b). These two leading modes account for 19.85% and 9.93% of the total variance. The spectrum analysis of the corresponding time series of the two leading modes shows that the $TEMP_{woGw}$ includes intraseasonal variability (Figure 2a, 2b). In the atmospheric forcing variable $TEMP_{woGwIs}$, the intraseasonal variability is eliminated (Figure 2c, 2d). The intrasesaonal variability has little effect on the spatial patterns of the two leading modes of the daily air temperature anomalies, except that removing the intraseasonal variability decreases the explained variance (Figure 1c, 1d).

We also apply an EOF analysis to the daily 10 m wind anomalies derived from ($UWND_{woGw}$, $VWND_{woGw}$) used in the CONTROL run and those derived from ($UWND_{woGwIs}$, $VWND_{woGwIs}$) used in the WOISALL run. Figure 3 shows spatial patterns of the two leading modes in the atmospheric variables ($UWND_{woGw}$, $VWND_{woGw}$) and those in the atmospheric variables ($UWND_{woGwIs}$, $VWND_{woGwIs}$). In the atmospheric forcing variable ($UWND_{woGw}$, $VWND_{woGw}$), wind anomalies for the AO pattern are characterized by the anomalous convergence/divergence centered in the central Arctic (Figure 3a). Wind anomalies for the AD pattern are characterized by the anomalous convergence/divergence centered in the Canadian Basin and anomalous divergence/convergence centered in the Barents Sea (Figure 3b). These two leading modes account for 14.86% and 12.11% of the total variance (Figure 3a, 3b). In the atmospheric forcing variable ($UWND_{woGwIs}$, $VWND_{woGwIs}$), the two leading modes account for 13.31% and 10.94% of the total variance (Figure 3c, 3d). Spectrum analysis of the corresponding time series of the two leading modes shows that the intraseasonal variability in sea surface wind speed data is effectively eliminated (not shown).

4. Results

4.1 Response of the Mean Sea Ice State

The 30-years-mean annual cycle of the simulated sea ice area and sea ice volume are shown in Figure 4. The sea ice area is the sum of the area of all the model grid cells weighted by the sea ice concentration. The sea ice area differences between the four simulations are small in March and relatively large in August-September (Figure 4a). Compared to the CONTROL and WOISALL runs, the WOISDYN run has the largest sea ice area in summertime, while the sea ice area in the WOISTHE run is the smallest in summertime. Although there is no intraseasonal variability in the forcing data used in the WOISALL run, the simulated sea ice area is still similar to that in the CONTROL run.

The spatial pattern of the simulated sea ice concentration in the CONTROL run and the deviations between the CONTROL and other runs are shown in Figure 5. In the CONTROL run, the sea ice extends from the central Arctic to the Bering Sea in the Pacific sector and to the Denmark Strait and the Labrador Sea in the Atlantic sector in March, with a maximum area of approximately 13.8 × 10^6 km^2. Sea ice appears in most of the Arctic marginal seas in September with a minimum area of approximately 6.5 × 10^6 km^2. Compared to the CONTROL run in March, the WOISTHE run presents a lower sea ice concentration near the sea ice edge in the Atlantic sector, with relatively large deviations in the Greenland Sea (Figure 5c). The simulated sea ice concentration over the sea ice edge regions in the WOISDYN run is higher in the Greenland Sea but lower in the Barents Sea (Figure 5e). By excluding both the atmospheric intraseasonal thermodynamical and dynamical variability, the simulated sea ice concentration over the sea ice edge regions in the WOISALL run is lower in the Barents Sea (Figure 5g). In September, compared to the CONTROL run, the WOISTHE run simulates lower sea ice concentration in whole basin with strong differences in the Arctic marginal seas (Figure 5d), the WOISDYN run simulates higher sea ice concentration in the Arctic marginal seas in the Eurasian Continent side but lower sea ice concentration in the southern Beaufort Sea and the Greenland Sea (Figure 5f), the WOISALL run simulates higher sea ice concentration in the East Siberia-Laptev Sea while lower sea ice concentration in the other marginal seas in the Arctic (Figure 5h).

Recovery of the sea ice area after a freezing season is somewhat independent of the sea ice coverage at the beginning of the freezing season, which involves the commonly referred “ice thickness-ice growth feedback” (Notz and Bitz, 2017), that is, thinner ice in later autumn supports larger conductive heat fluxes through the ice-air interface in the following winter and spring, and eventually leads to larger ice-growth rates, and thus the simulated sea ice area in March in the four simulations are quite similar. In contrast, the simulated sea ice volume shows substantial differences between the four simulations throughout the year (Figure 4b). The simulated sea ice volume in the WOISDYN run is larger than in the CONTROL run, with a maximum difference of approximately 1.0×10^3 km^3 in September. The sea ice volume in the WOISALL run is smaller than that in the CONTROL run, with a maximum difference of approximately 1.0×10^3 km^3 in April. The WOISTHE run presents the smallest sea ice volume compared to the other three simulations, with the minimum sea ice volume value of approximately 17.3×10^3 km^3 in September.

In the CONTROL run, the multi-year ice zone occupies the north of the Canadian Arctic Archipelago-Greenland Island and extends to the East Siberia Sea in March, with sea ice thickness larger than 3 m (Figure 6a). In September, the sea ice coverage with thickness larger than 3 m shrinks, and most of the Arctic marginal seas are covered by sea ice with thickness below 2 m (Figure 6b). The simulated sea ice thickness in the WOISTHE run is thinner than that in the CONTROL run (Figure 6c and 6d). Compared to the CONTROL run, in March, the simulated sea ice in the WOISDYN run is thicker in the central Arctic and the Laptev Sea and thinner in most of the Arctic marginal seas (Figure 6e). In September, compared to the CONTROL run, the simulated sea ice in the WOISDYN run is thinner in the southern Beaufort

Sea, the Greenland Sea, the northern Barents Sea and the northern Kara Sea but thicker in the central Arctic and the Laptev Sea (Figure 6f). In comparison with the CONTROL run, the simulated sea ice in the WOISALL run features thinner sea ice thickness in most of the Arctic marginal seas throughout the year (Figure 6g and 6h).

4.2 Causes of Sea Ice Area Adjustment based on Sea Ice Budget Analysis

In this section, we use sea ice budget analysis to investigate the physical processes that determine the evolution of the sea ice concentration in the simulations. In the sea ice model, each grid cell is divided into two subdomains: the open water domain and the ice-covered domain. In each cell, the change of sea ice concentration is determined by the atmospheric heat flux on the ice surface, the oceanic heat flux on the ice bottom, the atmospheric heat flux on the sea surface in the open water area, the sea ice advection, and the sea ice ridging process. The heat absorbed by the open water area in each cell is used for melting sea ice locally, and then the remaining heat can warm the ocean if all local sea ice has melted. As described in Liang et al. (2021), if we define a region with area A, the accumulated sea ice area increment (Δsia) over the time (t) can be expressed as:

$$\Delta sia = \langle \omega_{io} \rangle + \langle \omega_{ai} \rangle + \langle \omega_{ao} \rangle + \langle \omega_{advection} \rangle + \langle \omega_{ridge} \rangle \tag{1}$$

$$\omega_{advection} = \frac{\partial \psi_{advx}}{\partial x} + \frac{\partial \psi_{advy}}{\partial y} \tag{2}$$

where the subscripts (x, y) represent the two orthogonal axes in the model grid. (ψ_{advx}, ψ_{advy}) are the components of advection of sea ice concentration. ω_{io}, ω_{ai}, ω_{ao} and

$\omega_{advection}$ are the rates of change of sea ice concentration induced by the oceanic heat flux on the ice bottom, the atmospheric heat flux on the ice surface, the atmospheric heat flux on the sea surface in the open water area, and the sea ice advection, respectively. The operator <> represents the integral over area A and time t, that is, $<*>=\int_0^t \iint * \, dAdt$. $dA=dxdy$ and dt are the area and time element of the integration. In our simulations, the model states are saved on a daily basis, so that dt = 86400 s. ω_{io}, ω_{ai}, ω_{ao}, ψ_{advx}, and ψ_{advy} are directly saved by the model, and thereby $<\omega_{ridge}>$ can be calculated as the residual term.

Figure 7 shows the accumulated sea ice area increments over the whole model domain from March 15 to September 15 in the 30-years-mean climatology in the CONTROL run, as well as the differences between the CONTROL and other runs. As the lateral open boundaries of the model are far southward from the wintertime sea ice edge, $<\omega_{advection}>$ does not contribute to the change when $\omega_{advection}$ is integrated over the whole model domain. From March 15 to September 1, the sea ice area reductions in the WOISDYN, CONTROL, WOISALL, WOISTHE runs are 7.17 × 10^6 km^2, 7.26 × 10^6 km^2, 7.35 × 10^6 km^2, 7.45 × 10^6 km^2, respectively. In the CONTROL run (Figure 7a), the $<\omega_{ao}>$ term tends to increase sea ice area until May 10 with an accumulated sea ice area increment of 2 × 10^6 km^2, owing to that the cold air blows over the warm seawater and new ice continuously forms. After May 10, the $<\omega_{ao}>$ term tends to decrease sea ice area along with the rising of Arctic air temperature in summertime. The accumulated sea ice area increment owing to the $<\omega_{ao}>$ term from March 15 to September 1 is close to zero. The $<\omega_{io}>$ term always tends to decrease sea ice area due to the persistent upward oceanic heat transport at the ice bottom. The accumulated sea ice area loss due to the $<\omega_{io}>$ term reaches 1.7×10^6 km^2 until September 1. The $<\omega_{ai}>$ term contributes less to sea ice area reduction before May 1, thereafter plays a fueling role in sea ice area loss. The accumulated sea ice area loss due to the $<\omega_{ai}>$ term is comparable to that due to the $<\omega_{io}>$ term after July 15. The $<\omega_{ridge}>$ term contributes rather more to sea ice area loss, almost double of that due to the $<\omega_{io}>$ term.

The effect of atmospheric intraseasonal thermodynamic variability on sea ice area is dominated by its effect on the $<\omega_{ao}>$ term, with negligible effects on the $<\omega_{io}>$, $<\omega_{ai}>$, and $<\omega_{ridge}>$ terms (dashdot lines in Figure 7b). Compared to the WOISTHE run, the CONTROL run presents higher sea ice concentration in the Arctic marginal seas in summertime (Figure 5d), because the atmospheric intraseasonal thermodynamical forcing tends to reduce sea ice melting through changing the downward heat flux on the sea surface in the open water area, i. e., sea ice leads and polynyas. From March 15 to September 1, the retained sea ice area due to the $<\omega_{ao}>$ term originating from local atmospheric intraseasonal thermodynamical variability reaches approximate 0.14×10^6 km^2.

The intraseasonal atmospheric dynamical forcing has large partially compensating effects on the $<\omega_{ao}>$ and $<\omega_{ridge}>$ terms, and a small effect on the $<\omega_{io}>$ term (dotted lines in Figure 7b). Intraseasonal variability in the surface wind can perturb the sea ice and ocean motion, induces frequent variations in the open water area in the sea ice zone, which affects the sea ice area and volume through the $<\omega_{ao}>$

term. Intraseasonal variability in the surface wind can also result in frequent variations in the sea ice drift, affecting the sea ice area through the $<\omega_{ridge}>$ term. In addition, the intraseasonal variability in the surface wind and precipitation can affect vertical mixing and stratification in the upper ocean, and affect the sea ice by changed melting from below through the $<\omega_{io}>$ term. From March 15 to September 1 originating from local atmospheric intraseasonal dynamical variability, the retained sea ice area due to the $<\omega_{ao}>$ term, the disappeared sea ice area due to the $<\omega_{ridge}>$ and $<\omega_{io}>$ terms reach approximate 0.6×10^6 km^2, 0.59×10^6 km^2 and 0.18×10^6 km^2, respectively. As a result, the combined effects of all the sea ice budget terms show that the intraseasonal atmospheric dynamical variability tends to increase sea ice melting in the CONTROL run. With the combination of the intraseasonal atmospheric dynamical and thermodynamical variability (solid lines in Figure 7b), the total sea ice area of the CONTROL run in the September is larger than that of the WOISALL run.

Figure 8 shows spatial patterns of differences of the accumulated sea ice concentration increment terms from March 15 to September 15 between the CONTROL and WOISALL runs. The atmospheric intraseasonal variability strongly impedes sea ice concentration loss in the marginal seas through changing air-ocean heat flux, especially in the Greenland Sea, the northern Barents Sea, the Kara Sea, the Bering Sea and the southern Beaufort Sea (Figure 8a). The atmospheric intraseasonal variability strongly promotes sea ice concentration loss through strengthened dynamics-related ice ridging process in the regions near to islands and continental coasts (Figure 8d), and through enhanced oceanic heat flux, especially in the regions near to wintertime sea ice edge in the Greenland Sea, the Labrador Sea, and the Barents Sea (Figure 8c).

Although on the basin scale the sea ice area in the CONTROL run is lower that that in the WOISDYN run in September (Figure 4a), the sea ice concentration difference between the two runs shows a clear spatial pattern (Figure 5f). The intraseasonal atmospheric dynamical variability decreases the sea ice concentration in the East Siberia-Laptev Sea and increases the sea ice concentration in the Beaufort Sea and the Greenland Sea. In order to quantitatively assess the spatial distribution of the sea ice concentration differences, we further conducted a sea ice budget analysis for three regions (Figure 9) in the CONTROL and WOISDYN runs. Region A (RA) is the Beaufort Sea, Region B (RB) is the East Siberia-Laptev Sea, and Region C (RC) is the Greenland Sea.

In RA (Figure 10a), the $<\omega_{ao}>$ term leads to sea ice increase from March 15 to May 15, implying that the new ice continuously forms in the open water region. The sea ice area growth by the $<\omega_{ao}>$ term in the CONTROL run is larger than that in the WOISDYN run, implying that intraseasonal atmospheric dynamical variability favors the formation of new ice in the open water region. Intraseasonal variability in the surface wind can perturb the sea ice and ocean motion, create openings in which more ice could be formed, meanwhile new ice freezing in open water area also benefits from elevated turbulent heat exchange. The $<\omega_{ai}>$ term is almost 0 from March 15 to May 15, suggesting that the air-ice heat fluxes can not significantly affect sea ice area when the surface air temperature is much below the freezing point during this period, instead the energy would mostly just go into heating the ice up. The $<\omega_{ai}>$ term begins to contribute to the reduction of the sea ice concentration after May 15. Sea ice area reduction due to the $<\omega_{ai}>$ term in the CONTROL run is smaller than that in the WOISDYN run after June, indicating that the intraseasonal atmospheric dynamical variability reduces the sea ice surface melting by reduced downward air-ice heat fluxes through modifying the turbulent air-ice heat fluxes. The sea ice area reduction due to the $<\omega_{ridge}>$ term in the CONTROL run is larger than that in the WOISDYN run, indicating that intraseasonal atmospheric dynamical variability perturbs the sea ice motion, and leads to enhanced sea ice ridging activity. The $<\omega_{advection}>$ term tends to decrease the sea ice area before June 1 and increase the sea ice area after June 15.

Figure 11 shows the sea ice drift in May and August in the CONTROL and the deviations between the CONTROL and WOISDYN runs. The sea ice drift pattern in the WOISDYN run is similar to that in the CONTROL run, both in May and in August (not shown). In May, the spatial pattern of the sea ice drift in RA (Figure 11a) shows that sea ice advection tends to transport the sea ice out of RA, and thus the $<\omega_{advection}>$ term tends to decrease the sea ice area in May. In contrast, the spatial pattern of the sea ice drift in RA (Figure 11b) in August shows that sea ice advection integrated in RA tends to transport the sea ice into RA, and thus the $<\omega_{advection}>$ term tends to increase sea ice area in August. The sea ice drift deviations between the CONTROL and WOISDYN runs show that the intraseasonal atmospheric dynamical variability can induce an anticyclonic sea ice drift anomaly in the Beaufort Gyre region, and result in an enhanced Transpolar Drift in May (Figure 11c). In August, the intraseasonal atmospheric dynamical variability contributes less to the sea ice drift, just with a weaker anticyclonic sea ice drift anomaly restricted in the Beaufort Sea (Figure 11d). The sea ice area reduction in RA due to the $<\omega_{advection}>$ term in the CONTROL run is larger than that in the WOISDYN run before June 1, meaning that the intraseasonal atmospheric dynamical variability favors sea ice advection out of the RA before June 1. The combined effects of all these sea ice budget terms on the mean sea ice concentration increases sea ice concentration in September in the Beaufort Sea due to the intraseasonal atmospheric dynamical variability.

In RB (Figure 10b), the intraseasonal atmospheric dynamical variability induces a substantial decrease in the sea ice area, due to the decrease of sea ice concentration by the $<\omega_{ridge}>$, $<\omega_{advection}>$, $<\omega_{io}>$ terms exceeding the increase by the $<\omega_{ao}>$, $<\omega_{ai}>$ terms. In RC (Figure 10c), the intraseasonal atmospheric dynamical variability induces substantial increases of sea ice area as a result of the increase of sea ice by the $<\omega_{ao}>$, $<\omega_{advection}>$, $<\omega_{ai}>$ terms exceeding the decrease by the $<\omega_{io}>$, $<\omega_{ridge}>$ terms.

4.3 Effect on Sea Ice Intraseasonal Variability

As a first observation we note that the intraseasonal variability in sea ice concentration and thickness in the WOISTHE run are similar to those in the CONTROL run, and the intraseasonal variability in sea ice concentration and thickness in the WOISDYN run are also similar to those in the WOISALL run. Therefore, we focused on the comparison of sea ice intraseasonal variability between the CONTROL and WOISALL runs.

The intraseasonal variability of daily sea ice anomalies are calculated according to the following procedures, taking the simulated 30-years sea ice concentration at one of the grid points in the CONTROL run as an example: 1) calculate climatological annual cycle of sea ice concentration from the 30-years simulation. 2) remove the climatological annual cycle component from the 30-years simulation, and apply a band-pass filter algorithm based on a Chebyshev Type I filter to the residual to retain the variability with periods between 10 days and 90 days.

Figure 12 shows the standard deviations of the intraseasonal variability of the daily sea ice concentration and thickness anomalies. The strongest intraseasonal variability in the simulated sea ice concentration and thickness can be found in the marginal seas of the Arctic and in the sea ice edge regions. The amplitudes of intraseasonal variability of the sea ice concentration and thickness in the CONTROL run are significantly larger than that in the WOISALL run. The maximum amplitudes of intraseasonal variability of the daily sea ice concentration and thickness anomalies in the CONTROL run exceed 20% (Figure 12a) and 0.5 m (Figure 12b), respectively.

5. Discussion and Conclusion

From a systematic analysis of how the mean sea ice state in an Arctic sea ice-ocean model responds to prescribed atmospheric forcing with and without intraseasonal variability we find that the intraseasonal atmospheric thermodynamical variability tends to reduce sea ice melting through changing the downward heat flux on the open water area in the marginal sea ice zone, i.e. sea ice leads and polynyas.

The intraseasonal atmospheric dynamical variability has a large effect on the sea ice state and the upper ocean and tends to increase sea ice melting by a combination of modified air-ocean, ice-ocean heat fluxes and sea ice deformation. The September sea ice area driven by atmospheric forcing with intraseasonal variability is larger than that without intraseasonal variability, resulting from the intraseasonal atmospheric thermodynamical variability yielding a net sea ice area increase over the intraseasonal atmospheric dynamical variability in late summer.

In our experiment design, we simply classify air temperature, air humidity and radiative heat fluxes as thermodynamical variables, and classify wind components and precipitation as dynamical variables. This classification is chosen by considering the response time of sea ice and ocean to the atmospheric variables. The selected dynamical variables have a direct and long lasting influence on sea ice and ocean states, while the selected thermodynamical variables lead to a rapid and short-lived response of the sea ice and ocean states. However this classification is somewhat approximate, as it cannot fully isolate the atmospheric thermodynamical effect from the dynamical effect, because turbulent heat fluxes between air and sea ice are also related to wind speed. Besides, precipitation is a variable posing both dynamical and thermodynamical impacts on sea ice and ocean. It is noting that additional experiments reveal that the simulated sea ice area and volume in the WOISDYN and WOISTHE runs are not sensitive to the classification of precipitation in our model (not shown), which improves the rationality of the main findings in this study in some ways. Despite these classification difficulties, we believe that our results accurately represent the response of the sea ice mean state to intraseasonal variability in atmospheric thermodynamics and dynamics.

The intraseasonal variability of the atmospheric thermodynamical forcing has only small effects on sea ice and ocean dynamics. The reduced summertime sea ice melt can be mainly attributed to the reduced net heat flux into the surface ocean through ice leads. From our experiments it is difficult to disentangle the individual contributions of the thermodynamical forcing components of radiative heat flux, air temperature and humidity. Most of the dynamical forces acting on sea ice are intimately related to the surface winds. In our model, removing atmospheric intraseasonal variability in surface winds causes the mean sea ice motion to slow down. A likely explanation is that the missing wind power in this spectral band leads to reduced winds and thus reduced ice drift, which further leads to less ice deformation, and fewer leads or openings (parameterized by ice concentration). The ice strength remains stronger which further allows less or slower ice motion.

In view of the large spread in modeled sea ice area and volume in the CMIP models (Massonnet et al., 2018), it is an interesting question if this spread or at least part of it can be attributed to different representations of intraseasonal variability in the different CMIP models. In other words, our study implies that reliable modeling of atmospheric intraseasonal variability is an essential condition in correctly projecting future sea ice evolution. As the summertime sea ice extent and volume are likely to continuously decrease in the coming decades, more mobile sea ice will be even more subject to atmospheric forcing. As a consequence, the sea ice motion driven by Arctic atmospheric variability may become more intense (Olason and Notz, 2014).

We found in our numerical modeling study that atmospheric intraseasonal variability has a notable effect on the mean sea ice state. It would be exciting if it were possible to use observations to determine if this relationship also exists in the real Arctic. If this were possible, our findings could be extended to observed phenomena in the Arctic. It can be expected that intraseasonal atmospheric variability in a warming climate would play a more important role in accelerating sea ice melting in the Arctic marginal seas on the Eurasian continent side. Future works will focus on the changes of intraseasonal atmospheric variability under Arctic Amplification and its interactions with the underlying sea ice and ocean.

Acknowledgments. The authors thank the three anonymous reviewers for the constructive comments. This work is supported by the National Key R&D Program of China (2019YFE0105700, 2017YFE0111700). The authors thank the Japan Meteorological Agency for providing the JRA55 data (http://jra.kishou.go.jp/JRA-55/). The Arctic configuration of the MITgcm is available at https://github.com/oucliangxi/ArcticModel18km_MITGCM website.

References

Antonov, J. I., R. A. Locarnini, T. P. Boyer, A. V. Mishonov, and H. E. Garcia (2006), In S. Levitus (Ed.), World Ocean Atlas 2005, Volume 2: Salinity, NOAA Atlas NESDIS (Vol. 62, p. 182), Washington, DC: U.S. Government Printing Office.

Belchansky, G. I., D. C. Douglas, and N. G. Platonov (2004), Duration of the Arctic sea ice melt season: regional and interannual variability, 1979-2001. *J. Clim.,* **17(1)**, 67-80, doi:10.1175/1520-0442(2004)017<0067:DOTASI>2.0.CO;2.

Comiso, J. C. (2012), Large Decadal Decline of the Arctic Multiyear Ice Cover, *J. Clim.,* **25(4)**, 1176–1193, doi:10.1175/jcli-d-11-00113.1.

Deser, C., and H. Teng (2008), Evolution of Arctic sea ice concentration trends and the role of atmospheric circulation forcing 1979-2007, *Geophys. Res. Lett.,* **35(2)**, L02504, doi:10.1029/2007gl032023.

Deser, C., J. E. Walsh, and M. S. Timlin (2000), Arctic sea ice variability in the context of recent atmospheric circulation trends, *J. Clim.,* **13(3)**, 617-633, doi:10.1175/1520-0440(2000)013<0617:ASIVIT>2.0.CO;2.

Ding, Q., A. Schweiger, M. L'Heureux, D. S. Battisti, S. Po-Chedley, N. C. Johnson, E. Blanchard-Wrigglesworth, K. Harnos, Q. Zhang, R. Eastman, E. J. Steig (2017), Influence of high-latitude atmospheric circulation changes on summertime Arctic sea ice, *Nat. Clim. Change.,* **7(4)**, 289-295, doi:10.1038/nclimate3241.

Fang, Z., and J. M. Wallace (1994), Arctic sea ice variability on a timescale of weeks: Its relation to atmospheric forcing, *J. Clim.,* **7(12)**, 1897-1914, doi:10.1175/1520-0442(1994)007<1897:ASIVOA>2.0.CO;2.

Fetterer, F., K. Knowles, W. N. Meier, M. Savoie, and A. K. Windnagel (2017), Sea Ice Index, Version 3. Boulder, Colorado USA. NSIDC: National Snow and Ice Data Center, doi:10.7265/N5K072F8.

Francis, J. A. (2013), The where and when of wetter and drier: disappearing Arctic sea ice plays a role, *Envion. Res. Lett.,* **8(4)**, 041002, doi:10.1088/1748-9326/8/4/041002.

Frankignoul, C., N. Sennéchael, and P. Cauchy (2014), Observed Atmospheric Response to Cold Season Sea Ice Variability in the Arctic, *J. Clim.,* **27(3)**, 1243-1254, doi:10.1175/JCLI-D-13-00189.1.

Gao, Y., J. Sun, F. Li, S. He, S. Sandven, Q. Yan, Z. Zhang, K. Lohmann, N. Keenlyside, T. Furevik, and L. Suo (2015), Arctic sea ice and Eurasian climate: A review, *Adv. Atmos. Sci.,* **32(1)**, 92-114, doi:10.1007/s00376-014-0009-6.

Henderson, G. R., B. S. Barrett, and D. M. Lafleur (2014), Arctic sea ice and the Madden–Julian oscillation (MJO), *Clim. Dynam.,* **43**, 2185-2196, doi:10.1007/s00382-013-2043-y.

Harada, Y., H. Kamahori, C. Kobayashi, H. Endo, S. Kobayashi, Y. Ota, H. Onoda, K. Onogi, K. Miyaoka, and K. Takahashi (2016), The JRA-55 Reanalysis: Representation of atmospheric circulation and climate variability, *J. Meteor. Soc. Japan.,* **94(3)**, 269-302, doi:10.2151/jmsj.2016-015.

Hibler III, W. D. (1984), The role of sea ice dynamics in modelling CO2 increases, in Climate Processes and Climate Sensitivity, edited by J. E. Hansen, and T.

Takahashi, pp. 238-253, AGU, Washington, D. C.

Kobayashi, S., Y. Ota, Y. Harada, A. Ebita, M. Moriya, H. Onoda, K. Onogi, H. Kamahori, C. Kobayashi, H. Endo, K. Miyaoka, and K. Takahashi (2015), The JRA-55 Reanalysis: General specifications and basic characteristics, *J. Meteor. Soc. Japan.,* **93(1)**, 5-48, doi:10.2151/jmsj.2015-001.

Koenigk, T., U. Mikolajewicz, J. H. Jungclaus, and A. Kroll (2009), Sea ice in the Barents Sea: Seasonal to interannual variability and climate feedbacks in a global coupled model, *Clim. Dynam.,* **32(7-8)**, 1119-1138, doi:10.1007/s00382-008-0450-2.

Kwok, R., and D. A. Rothrock (1999), Variability of Fram Strait ice flux and North Atlantic Oscillation, *J. Geophys. Res.,* **104(C3)**, 5177-5189, doi:10.1029/1998jc900103.

Liang, X., and M. Losch (2018), On the effects of increased vertical mixing on the Arctic Ocean and sea ice, *J. Geophys. Res. Oceans.,* **123**, 9266-9282, doi:10.1029/2018JC014303.

Liang, X., X. Li, H. Bi, M. Losch, Y. Gao, F. Zhao, Z. Tian, and C. Liu (2021), A comparison of factors that led to the extreme sea ice minima in the 21st century in the Arctic Ocean. *J. Clim.*, accepted, doi: 10.1175/JCLI-D-21-0199.1.

Locarnini, R. A., A. V. Mishonov, J. I. Antonov, T. P. Boyer, and H. E. Garcia (2006), World Ocean Atlas 2005, Volume 1: Temperature. S. Levitus, Ed. NOAA Atlas NESDIS 61, U.S. Government Printing Office, Washington, D.C., 182 pp.

Losch, M., D. Menemenlis, J. M. Campin, P. Heimbach, and C. Hill (2010), On the formulation of sea-ice models. Part 1: Effects of different solver implementations and parameterizations, *Ocean Model.,* **33(1-2)**, 129-144, doi:10.1016/j.ocemod.2009.12.008.

Marshall, J., A. Adcroft, C. Hill, L. Perelman, and C. Heisey (1997), A finite-volume, incompressible Navier Stokes model for studies of the ocean on parallel computers, *J. Geophys. Res.,* **102(C3)**, 5753-5766, doi:10.1029/96JC02775.

Massonnet, F., M. Vancoppenolle, H. Goosse, D. Docquier, T. Fichefet, and E. Blanchard-Wrigglesworth (2018), Arctic sea-ice change tied to its mean state through thermodynamic processes, *Nat. Clim. Change.,* **8**, 599-603, doi: 10.1038/s41558-018-0204-z.

Meier, W. N., G. K. Hovelsrud, B. E. H. van Oort, J. R. Key, K. M. Kovacs, C. Michel, C. Haas, M. A. Granskog, S. Gerland, D. K. Perovich, A. Makshtas, and J. D. Reist (2014), Arctic sea ice in transformation: A review of recent observed changes and impacts on biology and human activity, *Rev. Geophys.,* **51**, doi:10.1002/2013RG000431.

Menemenlis, D., J. M. Campin, P. Heimbach, C. Hill, T. Lee, A. Nguyen, M. Schodlok, and H. Zhang (2008), ECCO2: High resolution global ocean and sea ice data synthesis, *Mercator Ocean Q. Newsl.,* **31**, 13-21.

Nguyen, A. T., D. Menemenlis, and R. Kwok (2011), Arctic ice-ocean simulation with optimized model parameters: Approach and assessment, *J. Geophys. Res. Oceans.,* **116**, 1-18, doi:10.1029/2010JC006573.

Notz, D. (2015), How well must climate models agree with observations? *Phil. Trans.*

R. Soc. A., **373**, 20140164, doi: 10.1098/rsta.2014.0164.

Notz, D., and C. M. Bitz (John Wiley & Sons, Chichester, 2017), in Sea Ice (ed. Tomas, D. N.).

Olason, E., and D. Notz (2014), Drivers of variability in Arctic sea-ice drift speed, *J. Geophys. Res. Oceans.,* **119**, 5755-5775, doi:10.1002/2014JC009897.

Qian, S., L. Zhang, B. Yang, A. Huang, and Y. Zhang (2020), Analysis of intraseasonal oscillation characteristics of Arctic summer sea ice, *Geophys. Res. Lett.,* **47(5)**, 1-8, doi:10.1029/2019GL086555.

Rigor, I. G., J. M. Wallace, and R. L. Colony (2002), Response of sea ice to the Arctic Oscillation, *J. Clim.,* **15**, 2648-2663, doi:10.1175/1520-0442(2002)0152.0.CO;2.

Smith, W. H., and D. Sandwell (1997), Global sea floor topography from satellite altimetry and ship depth soundings, *Science,* **277(5334)**, 1956-1962, doi:10.1126/science.277.5334.1956.

Strong, C. (2012), Atmospheric influence on Arctic marginal ice zone position and width in the Atlantic sector, February-April 1979-2010, *Clim. Dynam.,* **39(12)**, 3091-3102, doi:10.1007/S00382‑012‑1356‑6.

Thompson, D. W., and J. M. Wallace (1998), The Arctic Oscillation signature in the wintertime geopotential height and temperature fields, *Geophys. Res. Lett.,* **25(9)**, 1297-1300, doi:10.1029/98gl00950.

Wang, J., J. Zhang, E. Watanabe, M. Ikeda, K. Mizobata, J. E. Walsh, X. Bai, and B. Wu (2009), Is the Dipole Anomaly a major driver to record lows in Arctic summer sea ice extent? *Geophys. Res. Lett.,* **36(5)**, L05706, doi:10.1029/2008GL036706.

Watanabe, E., J. Wang, A. Sumi, and H. Hasumi (2006), Arctic dipole anomaly and its contribution to sea ice export from the Arctic Ocean in the 20th century, *Geophys. Res. Lett.,* **33(23)**, L23703, doi:10.1029/2006gl028112.

Yu, L., and S. Zhong (2018), Changes in sea-surface temperature and atmospheric circulation patterns associated with reductions in Arctic sea ice cover in recent decades, *Atmos. Chem. Phys.,* **18(19)**, 14149-14159, doi:10.5194/acp-18-14149-2018.

Zhang, J., and W. D. III. Hibler (1997), On an efficient numerical method for modeling sea ice dynamics, *J. Geophys. Res.,* **102(C4)**, 8691-8702, doi:10.1029/96JC03744.

Figure Captions

Figure 1. Spatial patterns of (a) the first- and (b) the second-leading EOF modes of daily 2 m air temperature anomalies derived from $TEMP_{woGw}$ used in the CONTROL run, (c) the first- and (d) the second-leading EOF modes of daily 2 m air temperature anomalies derived from $TEMP_{woGwIs}$ used in the WOISALL run. The number in each panel shows the percentage of variance explained by the mode.

Figure 2. Amplitude spectrum of time series of (a) the first- and (b) the second-leading EOF modes of daily 2 m air temperature anomalies derived from $TEMP_{woGw}$ used in the CONTROL run, (c) the first- and (d) the second-leading EOF modes of daily 2 m air temperature anomalies derived from $TEMP_{woGwIs}$ used in the WOISALL run. Spectrum amplitudes with oscillation period larger than 128 days are not shown. The red lines show the 95% confidence level.

Figure 3. Same as Figure 1 but for 10 m wind. Unit of the contour is m s^{-1}. Reference arrow is 0.5 m s^{-1}.

Figure 4. The 30-years-mean annual cycle of (a) sea ice area in 10^6 km^2 and (b) sea ice volume in 10^3 km^3. The black, red, blue, and cyan lines represent the CONTROL, WOISALL, WOISTHE, and WOISDYN runs, respectively.

Figure 5. Monthly mean sea ice concentration in the CONTROL run and the

deviations between the CONTROL and other runs. Left and right columns show the sea ice concentration in March and in September, respectively. Rows from top to bottom show the sea ice concentration in the CONTROL run, the deviations between the CONTROL and WOISTHE runs, the deviations between the CONTROL and WOISDYN runs, the deviations between the CONTROL and WOISALL runs, respectively.

Figure 6. Same as Figure 5 but for sea ice thickness. Unit is meters.

Figure 7. (a) Accumulated sea ice area increments from March 15 in the CONTROL run, (b) Difference of the accumulated sea ice area increments between the CONTROL run and the other runs. The black, blue, green, cyan and red lines represent the accumulated sea ice area increments due to the Δsia, $<\omega_{io}>$, $<\omega_{ai}>$, $<\omega_{ao}>$, and $<\omega_{ridge}>$ terms, respectively. The solid, dotted, and dashdot lines in (b) represents the WOISALL, WOISDYN, and WOISTHE runs, respectively. Unit is 10^6 km^2.

Figure 8. Spatial patterns of differences of the accumulated sea ice concentration increments from March 15 to September 15 between the CONTROL and WOISALL runs. (a)-(e) denote patterns corresponding to the $<\omega_{ao}>$, $<\omega_{ai}>$, $<\omega_{io}>$, $<\omega_{ridge}>$, and Δsia terms, respectively.

Figure 9. Domains of three regions (quadrangles) for sea ice budget analysis. The colors express the September sea ice concentration deviation between the CONTROL and WOISDYN runs. RA = Region A. RB = Region B. RC = Region C.

Figure 10. Accumulated sea ice area increments from March 15 in (a) RA, (b) RB, (c) RC in the CONTROL run (solid lines) and in the WOISDYN run (dashed lines). The black, blue, green, cyan, red and magenta lines represent the accumulated sea ice area increments due to the Δsia, $<\omega_{io}>$, $<\omega_{ai}>$, $<\omega_{ao}>$, $<\omega_{ridge}>$, and $<\omega_{advection}>$ terms, respectively. Unit is 10^6 km^2.

Figure 11. Monthly mean sea ice drift in the CONTROL run (top panels), and the deviations between the CONTROL and WOISDYN runs (bottom panels). Left and right columns show the sea ice drift in May and in August, respectively. Unit of the contour is m s^{-1}. Reference arrows for top and bottom panels are 0.05 m s^{-1} and 0.02 m s^{-1}.

Figure 12. Standard deviations of intraseasonal variability in daily sea ice concentration (left panels) and thickness (right panels) anomalies in meters. Top and bottom panels denote the CONTROL and WOISALL runs.

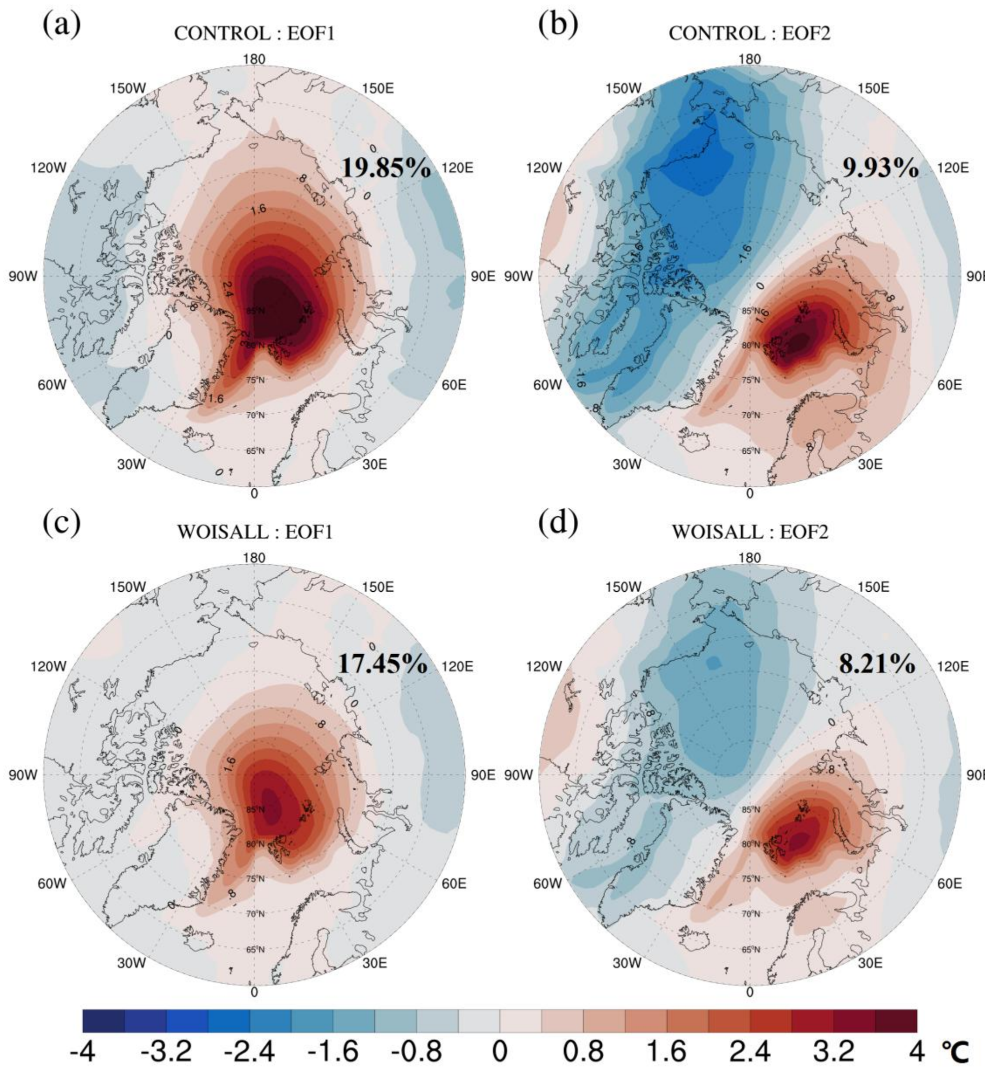

Figure 1. Spatial patterns of (a) the first- and (b) the second-leading EOF modes of daily 2 m air temperature anomalies derived from $TEMP_{woGw}$ used in the CONTROL run, (c) the first- and (d) the second-leading EOF modes of daily 2 m air temperature anomalies derived from $TEMP_{woGwIs}$ used in the WOISALL run. The number in each panel shows the percentage of variance explained by the mode.

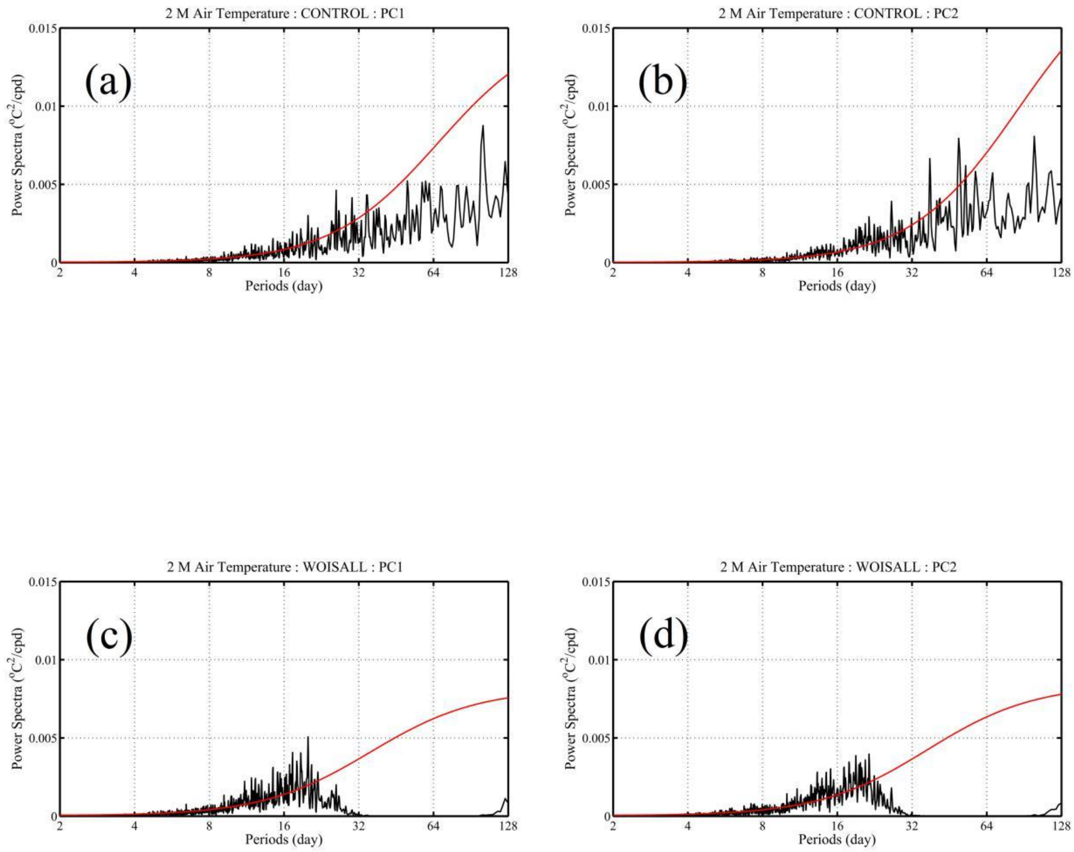

Figure 2. Amplitude spectrum of time series of (a) the first- and (b) the second-leading EOF modes of daily 2 m air temperature anomalies derived from $TEMP_{woGw}$ used in the CONTROL run, (c) the first- and (d) the second-leading EOF modes of daily 2 m air temperature anomalies derived from $TEMP_{woGwIs}$ used in the WOISALL run. Spectrum amplitudes with oscillation period larger than 128 days are not shown. The red lines show the 95% confidence level.

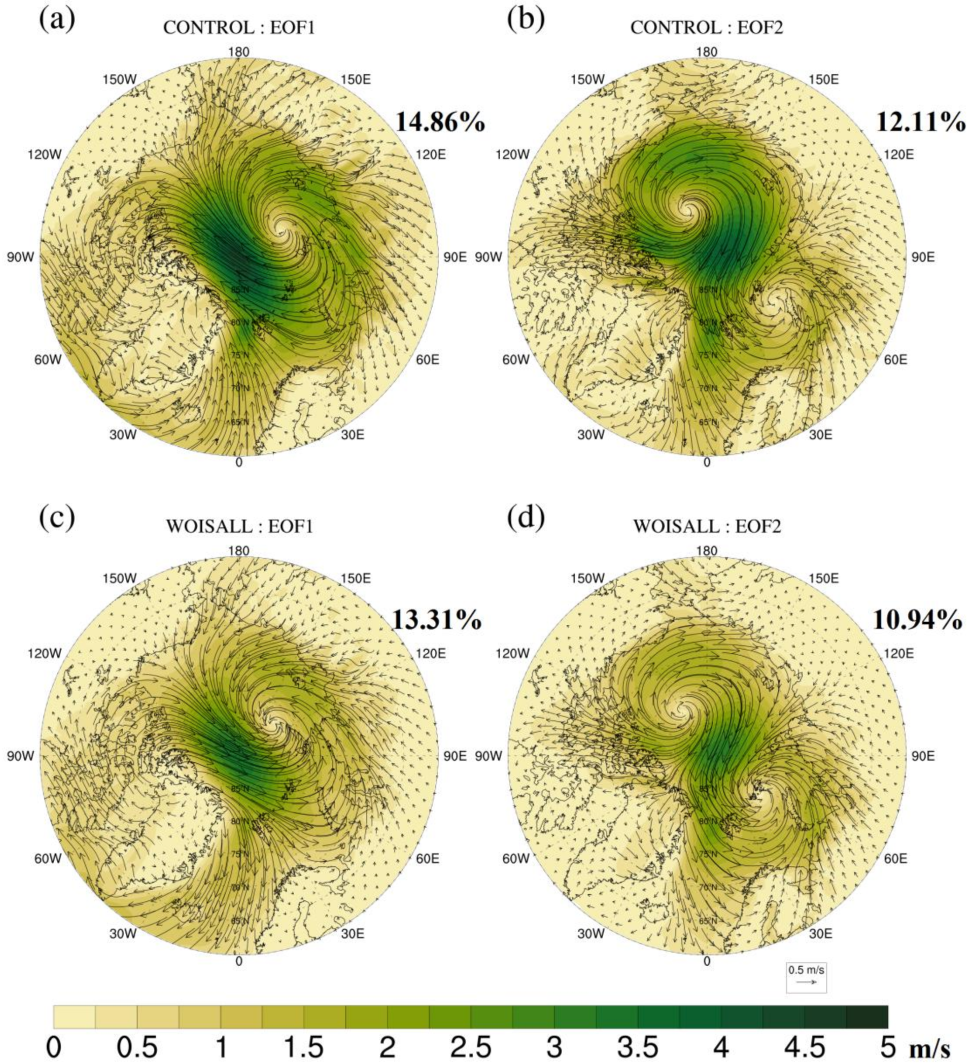

Figure 3. Same as Figure 1 but for 10 m wind. Unit of the contour is m s^{-1}. Reference arrow is 0.5 m s^{-1}.

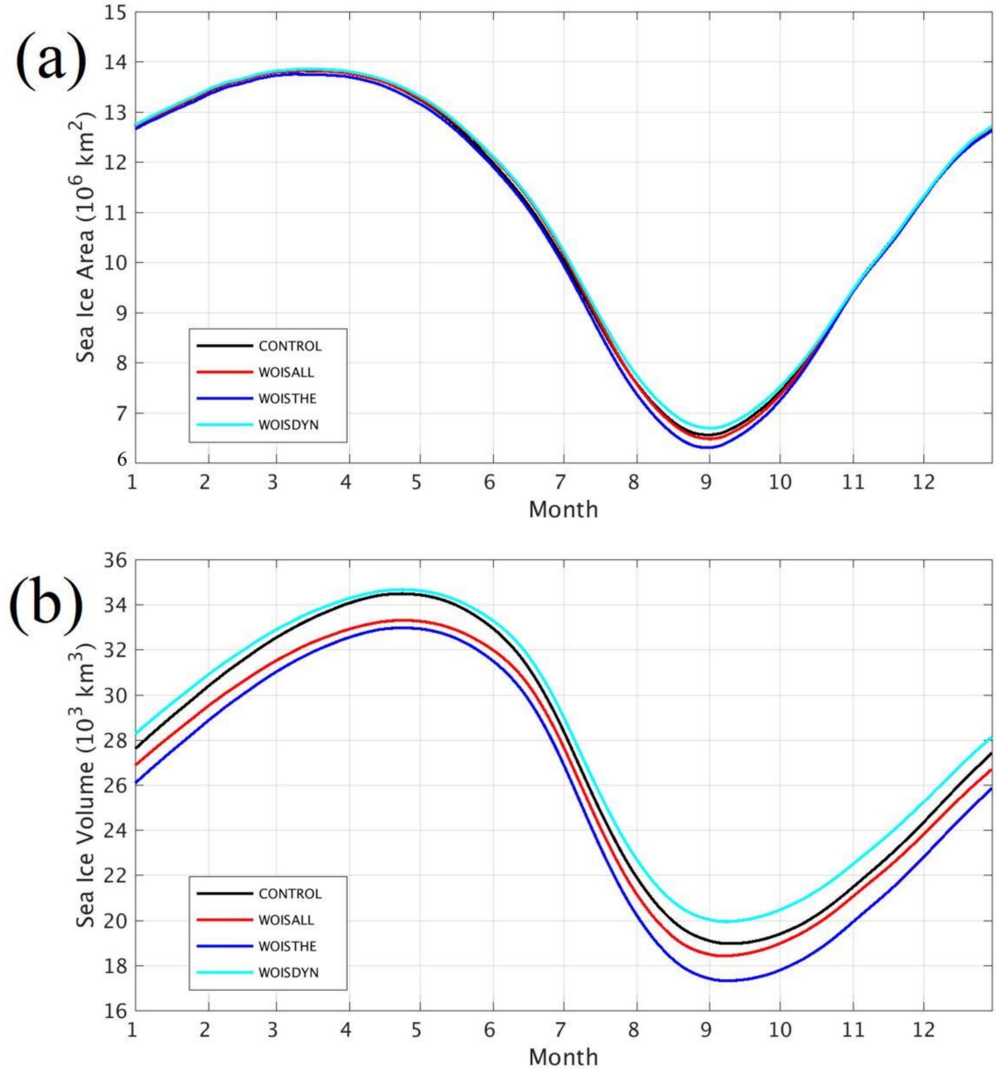

Figure 4. The 30-years-mean annual cycle of (a) sea ice area in 10^6 km^2 and (b) sea ice volume in 10^3 km^3. The black, red, blue, and cyan lines represent the CONTROL, WOISALL, WOISTHE, and WOISDYN runs, respectively.

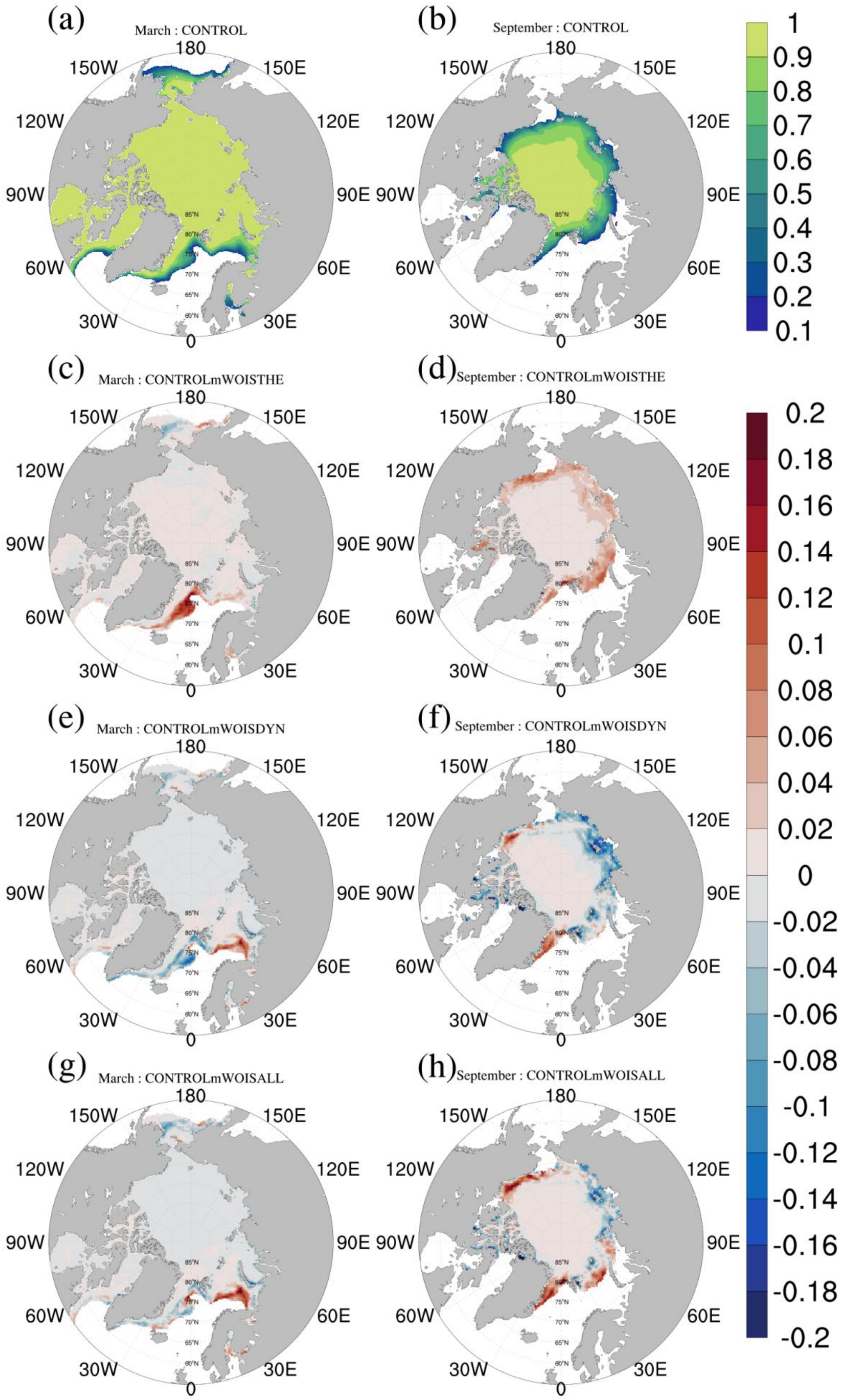

Figure 5. Monthly mean sea ice concentration in the CONTROL run and the deviations between the CONTROL and other runs. Left and right columns show the

sea ice concentration in March and in September, respectively. Rows from top to bottom show the sea ice concentration in the CONTROL run, the deviations between the CONTROL and WOISTHE runs, the deviations between the CONTROL and WOISDYN runs, the deviations between the CONTROL and WOISALL runs, respectively.

753

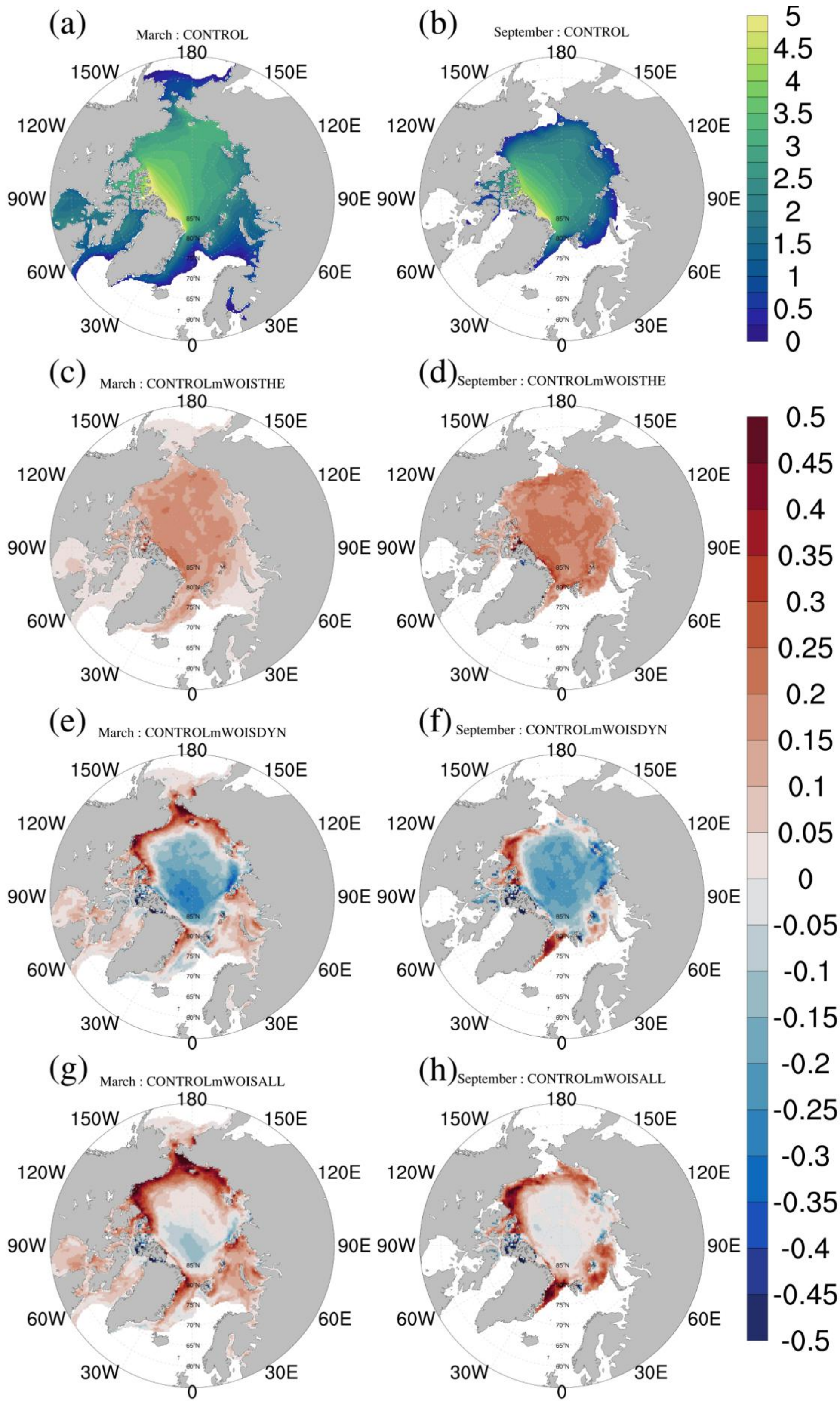

754 Figure 6. Same as Figure 5 but for sea ice thickness. Unit is meters.

755

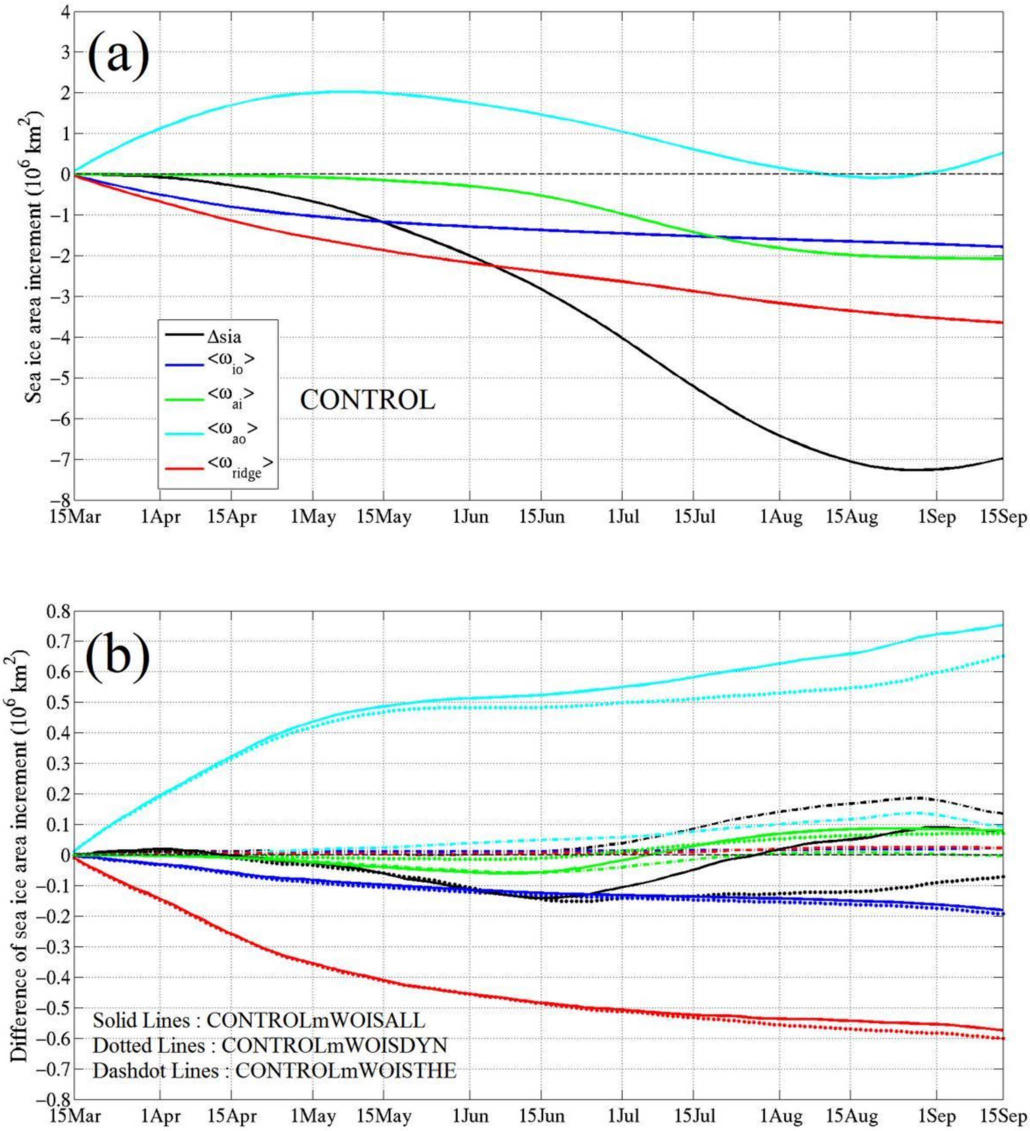

Figure 7. (a) Accumulated sea ice area increments from March 15 in the CONTROL run, (b) Difference of the accumulated sea ice area increments between the CONTROL run and the other runs. The black, blue, green, cyan and red lines represent the accumulated sea ice area increments due to the Δsia, $<\omega_{io}>$, $<\omega_{ai}>$, $<\omega_{ao}>$, and $<\omega_{ridge}>$ terms, respectively. The solid, dotted, and dashdot lines in (b) represents the WOISALL, WOISDYN, and WOISTHE runs, respectively. Unit is 10^6 km^2.

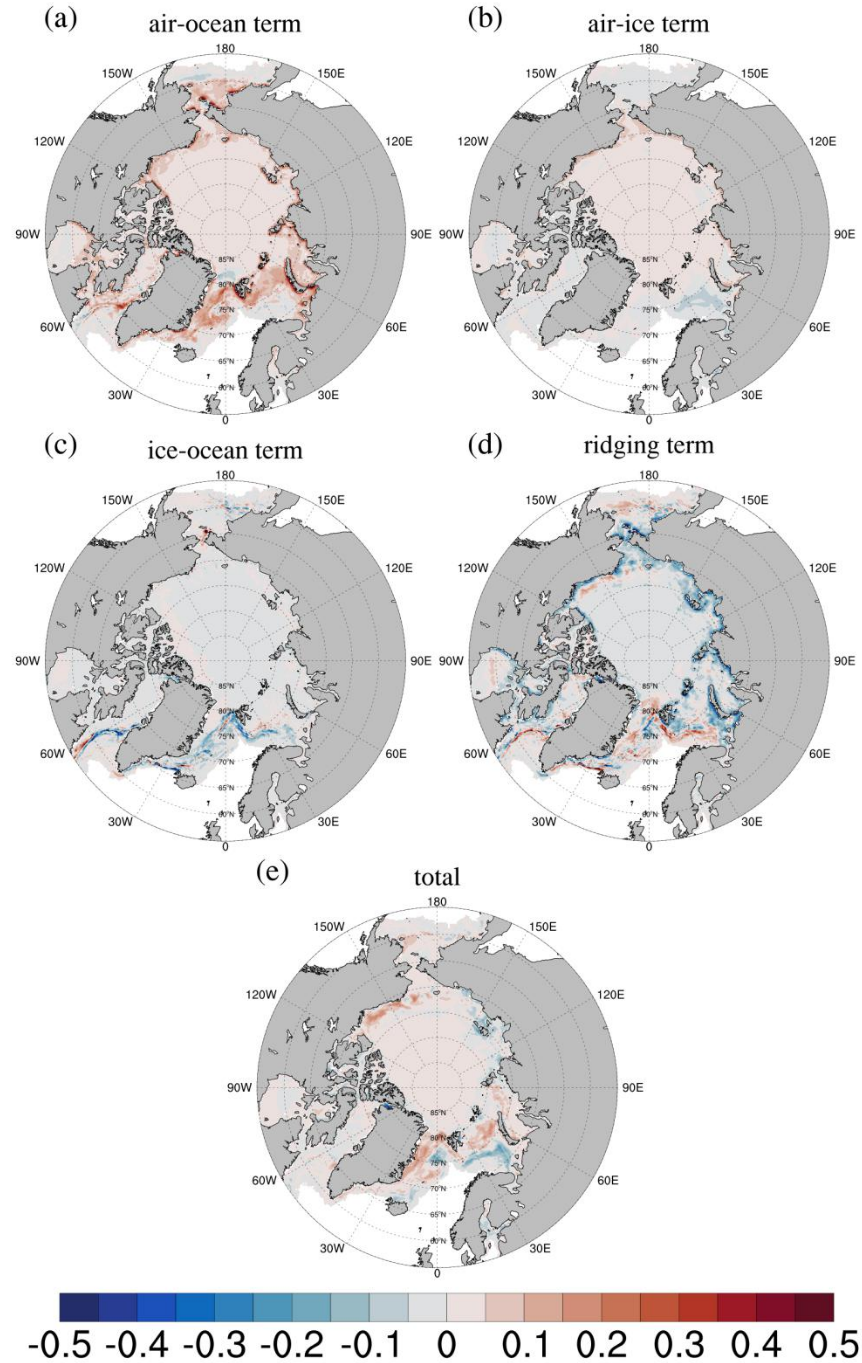

Figure 8. Spatial patterns of differences of the accumulated sea ice concentration increments from March 15 to September 15 between the CONTROL and WOISALL runs. (a)-(e) denote patterns corresponding to the <ω_{ao}>, <ω_{ai}>, <ω_{io}>, <ω_{ridge}>, and Δsia terms, respectively.

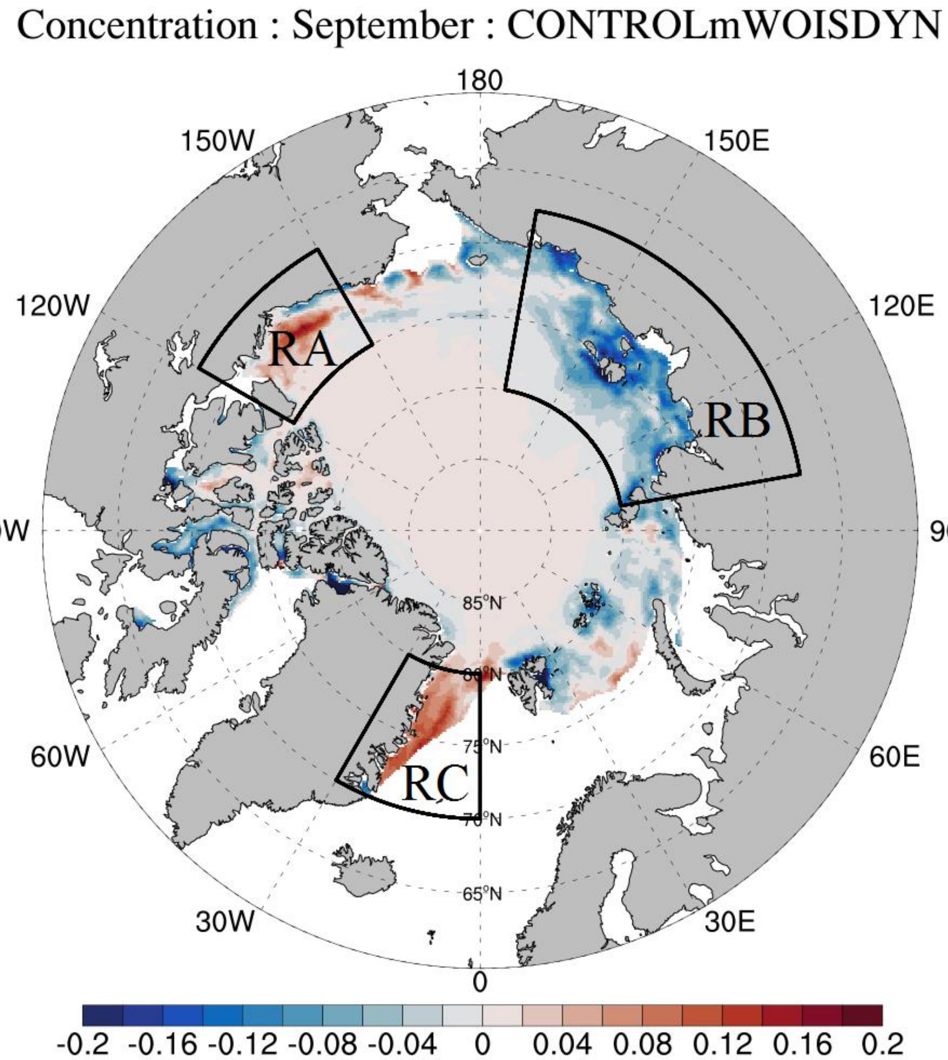

Figure 9. Domains of three regions (quadrangles) for sea ice budget analysis. The colors express the September sea ice concentration deviation between the CONTROL and WOISDYN runs. RA = Region A. RB = Region B. RC = Region C.

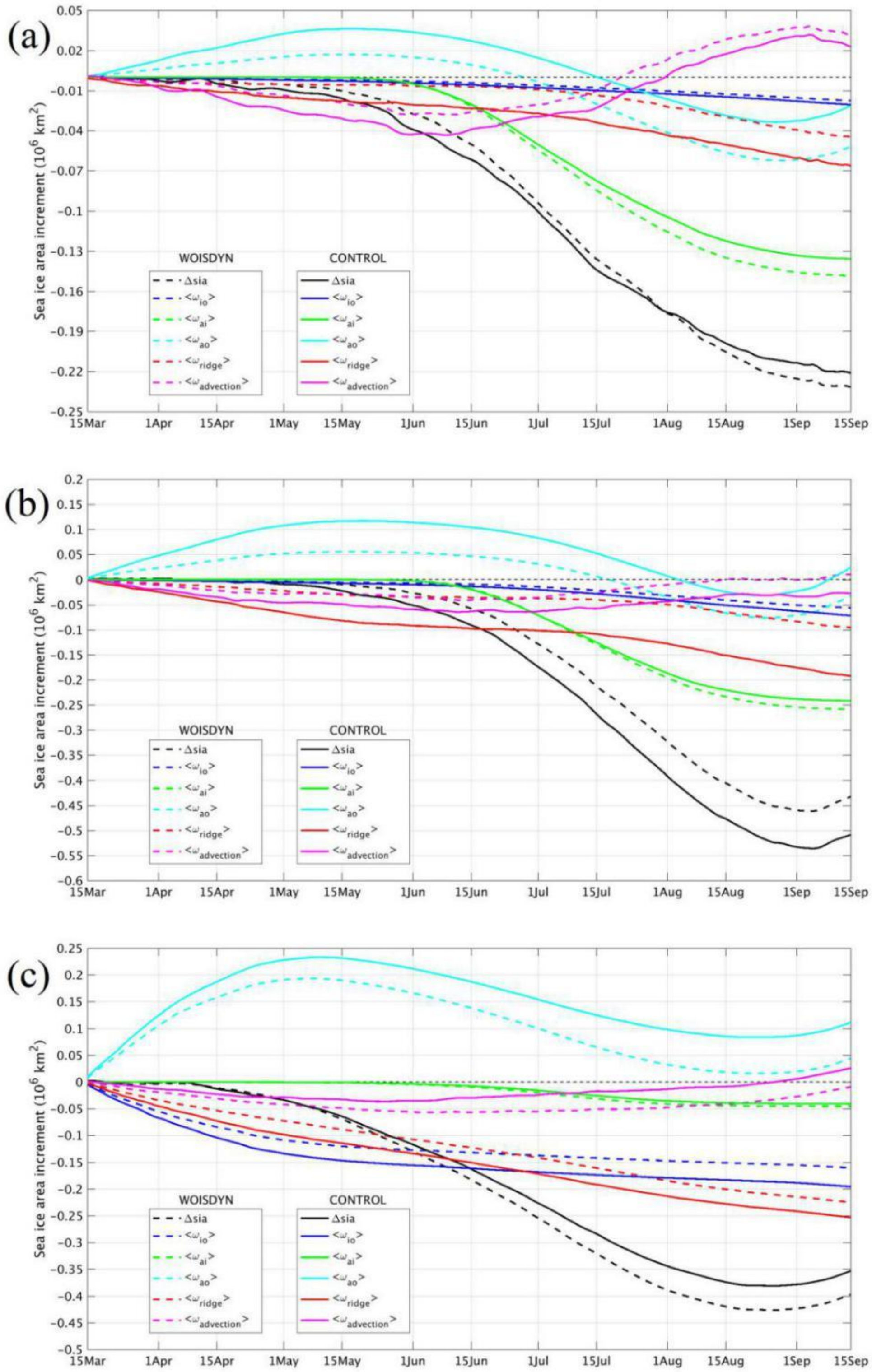

Figure 10. Accumulated sea ice area increments from March 15 in (a) RA, (b) RB, (c) RC in the CONTROL run (solid lines) and in the WOISDYN run (dashed lines). The black, blue, green, cyan, red and magenta lines represent the accumulated sea ice area

increments due to the Δsia, $<\omega_{io}>$, $<\omega_{ai}>$, $<\omega_{ao}>$, $<\omega_{ridge}>$, and $<\omega_{advection}>$ terms, respectively. Unit is 10^6 km^2.

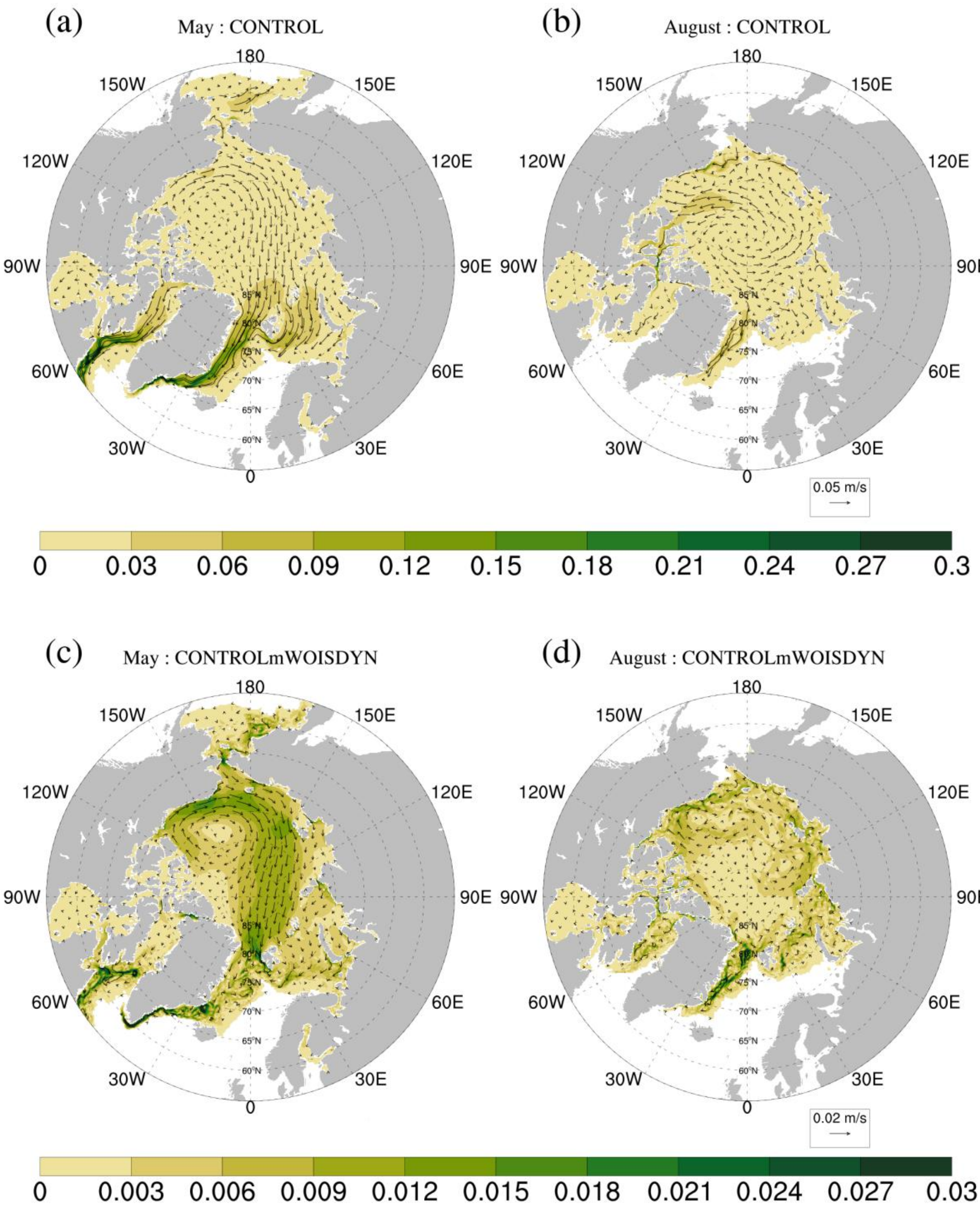

Figure 11. Monthly mean sea ice drift in the CONTROL run (top panels), and the deviations between the CONTROL and WOISDYN runs (bottom panels). Left and right columns show the sea ice drift in May and in August, respectively. Unit of the contour is m s^{-1}. Reference arrows for top and bottom panels are 0.05 m s^{-1} and 0.02 m s^{-1}.

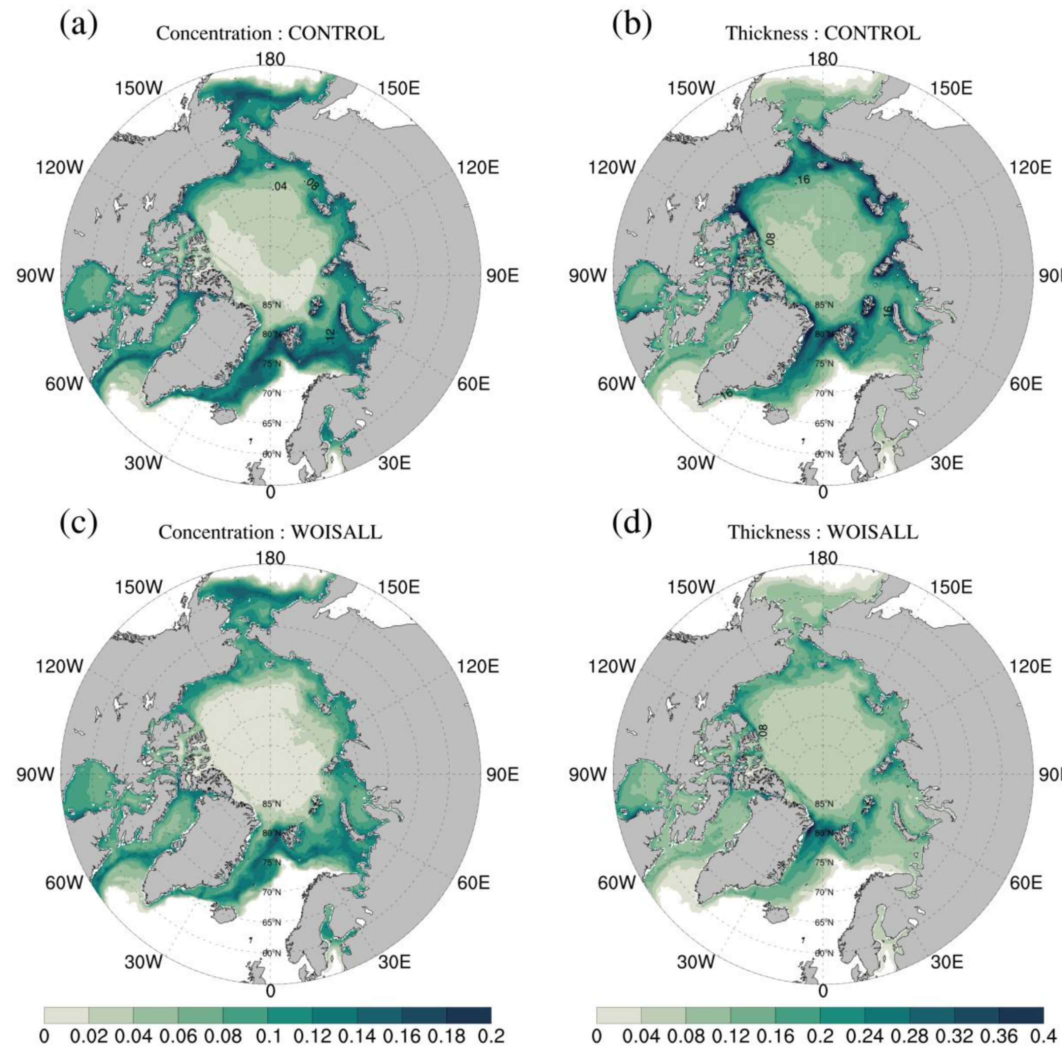

Figure 12. Standard deviations of intraseasonal variability in daily sea ice concentration (left panels) and thickness (right panels) anomalies in meters. Top and bottom panels denote the CONTROL and WOISALL runs.

Table 1. Description of atmospheric data appeared in section 2.2. *VAR* includes 7 variables: *TEMP* (2 m air temperature), *HUMI* (2 m air specific humidity), *UWND* (10 m wind u component), *VWND* (10 m wind v component), *RAIN* (precipitation), *SWHF* (downward shortwave heat flux at sea surface), *LWHF* (downward longwave heat flux at sea surface).

Symbol	Data Length (years)	Description
$VAR_{79\text{-}13}$	35	3 hourly JRA55 variables
VAR_{Ac}	1	climatological annual cycle data with 3 hourly temporal resolution
VAR_{woAc}	35	3 hourly JRA55 variables without annual cycle component
VAR_{Gw}	35	Long-term trend (global warming component) in the 3 hourly JRA55 variables
VAR_{woAcGw}	35	3 hourly JRA55 variables without annual cycle and global warming components
VAR_{woGw}	35	3 hourly JRA55 variables without global warming component.
$VAR_{woAcGwIs}$	35	3 hourly JRA55 variables without annual cycle and global warming components, and without intraseasonal oscillation components in regions north of 60 °N.

VAR_{woGwIs}	35	3 hourly JRA55 variables without global warming component, and without intraseasonal oscillation components in regions north of 60 °N.

Table 2. Description of experiment design. *VAR* includes 7 variables: *TEMP* (2 m air temperature), *HUMI* (2 m air specific humidity), *UWND* (10 m wind u component), *VWND* (10 m wind v component), *RAIN* (precipitation), *SWHF* (downward shortwave heat flux at sea surface), *LWHF* (downward longwave heat flux at sea surface).

Experiment	Data Length (years)	Atmospheric Variables	Intraseasonal Atmospheric Variability	
			Thermodynamical	Dynamical
CONTROL	35	VAR_{woGw} *for all 7 variables*	*Yes*	*Yes*
WOISALL	35	VAR_{woGwIs} *for all 7 variables*	*No*	*No*
WOISTHE	35	VAR_{woGwIs} *for (TEMP, HUMI, SWHF, LWHF)* VAR_{woGw} *for (UWND, VWND, RAIN)*	*No*	*Yes*
WOISDYN	35	VAR_{woGwIs} *for (UWND, VWND, RAIN)* VAR_{woGw} *for (TEMP, HUMI, SWHF, LWHF)*	*Yes*	*No*